Poisson equation for weak gravitational lensing

Thomas P. Kling* and Bryan Campbell†
Dept. of Physics, Bridgewater State College, Bridgewater, MA 02325
(Dated: June 17, 2008)

Using the Newman & Penrose [1] spin coefficient (NP) formalism, we examine the full Bianchi identities of general relativity in the context of gravitational lensing, where the matter and space-time curvature are projected into a lens plane perpendicular to the line of sight. From one component of the Bianchi identity, we provide a rigorous, new derivation of a Poisson equation for the projected matter density where the source term involves second derivatives of the observed weak gravitational lensing shear. We also show that the other components of the Bianchi identity reveal no new results. Numerical integration of the Poisson equation in test cases shows an accurate mass map can be constructed from the combination of a ground-based, wide-field image and a Hubble Space Telescope image of the same system.

PACS numbers: 98.62.Sb, 95.30.-k, 95.30.Sf, 04.90.+e

arXiv:0806.2834v1 [gr-qc] 17 Jun 2008

I. INTRODUCTION

In the current age of precision cosmology, weak gravitational lensing is an important tool in understanding cluster mass morphology. Because all gravitating mass (baryonic or dark) influences the path of light rays on the same footing, gravitational lensing studies are the most direct measure of mass distribution within galaxies or galaxy clusters.

Current weak gravitational lensing studies relate the projected matter distribution to the observed gravitational shearing of images through an integral relation derived in Miralda-Escude [2] and elsewhere. Previous work by Seitz et al. [3] and others introduces a PDE approach where the gravitational shearing is related first to the gravitational potential, from which the underlying matter distribution can be found.

A recent paper by Kling & Keith [4] introduced a new PDE approach to weak gravitational lensing that directly relates the gravitational shear to the projected matter distribution. By examining the weak gravitational perturbations on a flat background space-time in the NP spin coefficient formalism for a tetrad of constant null vectors, Kling & Keith [4] showed that one component of the Bianchi identity provides a first-order, complex partial differential equation relating the gravitational shearing of images to the projected matter density. Using a Green's function, the authors were able to show that their PDE was equivalent to the integral equation derived by Miralda-Escude [2].

This paper provides a more detailed derivation of the relevant PDE to first order in gravitational potential and using a non-constant NP null tetrad. To this order, we show that the other components of the Bianchi identity (that were not examined in Kling & Keith [4]) yield no new information related to gravitational lensing. We show that a real Poisson equation naturally arises from this complex, first-order PDE that relates the gravitational shear to the projected matter density. The Poisson equation derived here is related to the Poisson equation of Seitz et al. [3], but is derived from first principles of general relativity.

We numerically integrate the Poisson equation using relaxation methods for a matter distribution representing a truncated, isothermal sphere with a core radius. These numerical integrations are used to study the feasibility of the method for application to observational scenarios.

II. NP FORMALISM

In this section, we explain the physical arrangement of an observer, sources and matter distribution that leads to the null tetrad at the heart of the NP formalism. We then specify Ricci and Weyl tensor components and non-zero spin coefficients and list the Bianchi identities in the NP formalism.

---

*Electronic address: tkling@bridgew.edu
†Sponsored by the Adrian Tinsley Program for Undergraduate Research, BSC

A. Matter distribution and tetrad

We begin by considering an observer at the origin in a weakly perturbed, flat Robertson-Walker (RW) space-time. We assume that the perturbation is localized in some region far from the observer and that light sources lie beyond the perturbation, near the line of sight. We assume that these sources do not influence the space-time metric. For simplicity, we take the center of the matter distribution that perturbs the metric to lie at some distance along the $-\hat{z}$ axis. The space-time metric takes the form

$$d\tilde{s}^2 = (1+2\varphi)\, d\tilde{t}^2 - a(\tilde{t})^2(1-2\varphi)\{dx^2+dy^2+dz^2\}, \tag{1}$$

where the perturbation φ depends on the proper distance in the background RW metric at the time light rays from the sources pass the lens on their way to the observer. The metric, Eq. 1 is conformal to the static metric

$$ds^2 = (1+2\varphi)\, dt^2 - (1-2\varphi)\{dx^2+dy^2+dz^2\}, \tag{2}$$

and the light rays of the two metrics are identical.

The NP spin coefficient formalism is based on a tetrad of null vectors,

$$\lambda^a_i = \{\ell^a, n^a, m^a, \bar{m}^a\}\,, \tag{3}$$

where m^a and $\bar{m}^a$ are complex spatial vectors spanning the cross section of a pencil of light rays and ℓ^a and n^a are real null vectors. The tetrad vectors satisfy $\ell^a n_a = 1$ and $m^a \bar{m}_a = -1$ with all other products equal to zero. The first null vector, ℓ^a, is chosen to be tangent to the past-directed null geodesics.

For our purposes, we will be considering null geodesics that connect our observer at the origin with sources lying beyond the lens near the $-\hat{z}$ axis. Since we are pursuing weak gravitational lensing to first order in the gravitational potential, we will assume that the null geodesics connecting the observer and source are those of the background metric

$$ds^2 = dt^2 - \{dx^2+dy^2+dz^2\}. \tag{4}$$

Variations in these null geodesics would be first order corrections in the gravitational potential. Using the complex variable

$$\zeta = e^{i\phi}\cot\theta/2 = \frac{x+i\,y}{\sqrt{x^2+y^2+z^2}-z}, \tag{5}$$

we can write the cartesian coordinate components of null tetrad vectors as

$$\ell^a = \frac{1}{\sqrt{2}(1+\zeta\bar{\zeta})}\left(-1-\zeta\bar{\zeta}, \zeta+\bar{\zeta}, i(\bar{\zeta}-\zeta), -1+\zeta\bar{\zeta}\right), \tag{6}$$

$$n^a = \frac{1}{\sqrt{2}(1+\zeta\bar{\zeta})}\left(-1-\zeta\bar{\zeta}, -(\zeta+\bar{\zeta}), i(\zeta-\bar{\zeta}), 1-\zeta\bar{\zeta}\right), \tag{7}$$

$$m^a = \frac{1}{\sqrt{2}(1+\zeta\bar{\zeta})}\left(0, 1-\bar{\zeta}^2, -i(\bar{\zeta}^2+1), 2\,\bar{\zeta}\right). \tag{8}$$

All of these vectors are null in the background metric, Eq. 4. When $\zeta = 0$, the spatial part of ℓ^a is aligned with the $-\hat{z}$ axis. n^a and m^a are parallel propagated in the background metric along the ℓ^a congruence. Geometrically, m^a is a complex spatial vector perpendicular to the spatial part of ℓ^a that lies in the cross section of the light bundle surrounding ℓ^a.

B. Spin coefficients and curvature tensors

The Ricci rotation coefficients are defined by

$$\gamma_{ijk} = \lambda_j^b \, \lambda_k^a \, \nabla_a \, \lambda_{i\,b}, \tag{9}$$

and in the NP formalism, these are arranged into twelve complex NP spin coefficients. In our examination of the Bianchi identity, we will assume that ζ is small so that the light rays lie close to the $-\hat{z}$ axis. The spin coefficients appear in the Bianchi identity multiplied by a Weyl or Ricci tensor component which we compute to first order in the perturbation, φ. Hence, we will keep only the zeroth order in ζ contribution to the spin coefficients. In the appendix, we show that the only non-zero spin coefficients to this order are

$$\rho = \mu = -\frac{1}{\sqrt{2}r}, \tag{10}$$

where $r^2 = x^2 + y^2 + z^2$.

The Ricci and Weyl tensors are decomposed into tetrad components by contracting the coordinate components with the tetrad vectors. We assume that the gravitational perturbation and ζ are small, and discard terms of the form $\zeta \times \varphi$. In the appendix, we find that the non-zero NP Ricci curvature components are

$$\Phi_{00} = \Phi_{22} = 2\Phi_{11} = \frac{1}{2}\nabla^2\varphi. \tag{11}$$

The first order Weyl tensor components are

$$\begin{aligned} \Psi_0 = \overline{\Psi}_4 &= \frac{1}{2}(\varphi_{xx} - \varphi_{yy} - 2i\varphi_{xy}) \\ \Psi_1 = -\overline{\Psi}_3 &= \frac{1}{2}(\varphi_{xz} - i\varphi_{yz}) \\ \Psi_2 &= \frac{1}{2}\left(\varphi_{zz} - \frac{1}{3}\nabla^2\varphi\right). \end{aligned} \tag{12}$$

The four directional derivatives associated with the null tetrad play an important role in the NP formalism and are given special names:

$$D = \ell^a\partial_a, \qquad \Delta = n^a\partial_a, \qquad \delta = m^a\partial_a, \qquad \bar{\delta} = \bar{m}^a\partial_a. \tag{13}$$

Since the potential is time independent, to zeroth order in ζ, these derivative operators act as

$$D = -\Delta = -\frac{1}{\sqrt{2}}\frac{\partial}{\partial z} \qquad \delta = \frac{1}{\sqrt{2}}\left(\frac{\partial}{\partial x} - i\frac{\partial}{\partial y}\right). \tag{14}$$

C. Bianchi identity

The Bianchi identity can be expressed in terms of the Ricci and Weyl tensor components, spin coefficients and the directional derivatives in eight complex equations [5]. A central purpose of this paper is to examine all of the Bianchi identity equations under the context of weak gravitational lensing. Here, we list the Bianchi identity components that relate the Ricci and Weyl curvature tensor components, keeping only terms which are first order φ and discarding terms of order $\zeta\varphi$.

$$\bar{\delta}\Psi_0 - D\Psi_1 - \delta\Phi_{00} = -4\rho\Psi_1 \tag{15}$$

$$\Delta\Psi_0 - \delta\Psi_1 = -\mu\Psi_0 \tag{16}$$

$$3(\bar{\delta}\Psi_1 - D\Psi_2) + 2D\Phi_{11} - \Delta\Phi_{00} = -9\rho\Psi_2 \quad (17)$$
$$3(\Delta\Psi_1 - \delta\Psi_2) - 2\delta\Phi_{11} = -6\mu\Psi_1 \quad (18)$$
$$3(\bar{\delta}\Psi_2 - D\Psi_3) + 2\bar{\delta}\Phi_{11} = -6\rho\Psi_3 \quad (19)$$
$$3(\Delta\Psi_2 - \delta\Psi_3) + D\Phi_{22} - 2\Delta\Phi_{11} = -9\mu\Psi_2 \quad (20)$$
$$\bar{\delta}\Psi_3 - D\Psi_4 = -\rho\Psi_4 \quad (21)$$
$$\Delta\Psi_3 - \delta\Psi_4 + \bar{\delta}\Phi_{22} = -4\mu\Psi_3 \quad (22)$$

These equations are trivial identities if one uses the definitions of the Ricci and Weyl curvature tensor components from the right hand sides of Eqs. 11 and 12.

Our purpose is to examine these equations as field equations, where we assume that we know the Weyl tensor components and wish to solve for the Ricci tensor components. To this end, we will use the equivalences of the left hand sides of Eqs. 11 and 12.

We note that this is the opposite of the program of Newman and Penrose, who studied gravitational radiation using these equations. There, vacuum space-time was studied so that the Ricci tensor was zero, and the Bianchi identities provided field equations to examine Weyl tensor components at infinity, which represented gravitational radiation.

III. WEAK GRAVITATIONAL LENSING

In gravitational lensing, the three-dimensional matter density that leads to the deflection of light is projected into a two-dimensional surface matter density in the "lens plane." The null geodesics connecting the observer and a source are replaced by two straight (asymptotic) rays that form a deflection angle at the lens plane. This leads to a lens equation mapping image locations in the lens plane into source positions in the source plane. The lens equation map depends on first derivatives (in the lens plane) of the projected gravitational potential. The Jacobian of this mapping involves second derivatives of the projected gravitational potential. This Jacobian can be used to map the shape of extended sources in the source plane into extended images in the lens plane, as is demonstrated in [6] and [7].

We define $\psi(x, y)$ as the projected gravitational potential,

$$\psi(x, y) = \int_o^s \varphi ds, \quad (23)$$

where the integral is taken from the observer position to the source position along the path connecting the source and observer. The projected gravitational potential depends only on the position the ray connecting the observer to the source strikes the lens plane (whose coordinates are x and y).

The goal of weak gravitational lensing is to determine the projected matter density, κ, from observed weak gravitational "shears:" γ_1 and γ_2. These three quantities arise in the Jacobian of the lens mapping and are defined as

$$\kappa = \frac{1}{2}(\psi_{xx} + \psi_{yy}) = \frac{1}{2}\Delta^2\psi \quad (24)$$
$$\gamma_1 = \frac{1}{2}(\psi_{xx} - \psi_{yy}) \;\; \& \;\; \gamma_2 = \psi_{xy}. \quad (25)$$

(Note that this matter density κ is unrelated to the spin-coefficient κ of Eq. A.5.) Using a Fourier transform technique, one can show that

$$\kappa(\vec{r}) = \int d\vec{r}' \, \frac{[\gamma_1(\vec{r}') \, , \, \gamma_2(\vec{r}')]}{\pi} \cdot \frac{[\cos 2\eta \, , \, \sin 2\eta]}{|\vec{r} - \vec{r}'|^2}, \quad (26)$$

where η is the angle between the two-dimensional position vectors $\vec{r}$ and $\vec{r}'$ in the lens plane. This integral equation is the basis for observational weak gravitational lensing.

IV. PROJECTION OF CURVATURE TENSORS

The connection of our NP formalism to gravitational lensing is accomplished by projecting each of our Bianchi identities and the relevant curvature components along the paths connecting the observer and source. While the

Bianchi identity relates curvature components at each point along the light ray connecting the source and observer, the projection represents an accumulation similar to that studied in gravitational lensing.

We begin by projecting the Ψ_0 and Φ_{00} curvature components. Since we are interested in weak lensing (where the deflection is minimal), we project by integrating along the spatial part of the past light rays given by ℓ^a in the tetrad, Eq. 6. Since we want to work to lowest order in the potential, this is equivalent to integrating along the z axis from the observer to the source. Using a pre-script "L" to denote a quantity projected into the lens plane, we define

$$ {}_L\Phi_{00} \equiv \int_{z_o}^{z_s} dz\, \Phi_{00} = \frac{1}{2}\left(\psi_{xx} + \psi_{yy}\right), \tag{27}$$

where we use Eq. 11 with Eq. 23 and the assumption that φ_z is zero far from the lens. Likewise, the Weyl tensor component Ψ_0 is projected as

$$ {}_L\Psi_0 \equiv \int_{z_o}^{z_s} dz\, \Psi_0 = \frac{1}{2}\left(\psi_{xx} - \psi_{yy} - 2i\psi_{xy}\right). \tag{28}$$

We see an immediate connection between the curvature tensor components and gravitational lensing: ${}_L\Phi_{00} = \kappa$ and ${}_L\Psi_0 = \gamma_1 - i\gamma_2$. In Kling & Keith [4], ${}_L\Phi_{00}$ and ${}_L\Psi_0$ are shown to obey an analogous integral relation to Eq. 26.

The remaining Ricci tensor components project as

$$ {}_L\Phi_{22} = 2\,{}_L\Phi_{11} = {}_L\Phi_{00} = \kappa. \tag{29}$$

Likewise, ${}_L\Psi_4 = {}_L\overline{\Psi}_0 = \gamma_1 + i\gamma_2$, but the projections of Ψ_1 and Ψ_3 are both zero because both involve a z derivative and we assume φ_x and φ_y are zero far from the lens. The projection of Ψ_2 is

$$ {}_L\Psi_2 \equiv \int_{z_o}^{z_s} dz\, \frac{1}{2}\left(\varphi_{zz} - \frac{1}{3}\nabla^2\varphi\right) = -\frac{1}{6}\left(\psi_{xx} + \psi_{yy}\right) = -\frac{1}{3}\kappa. \tag{30}$$

That the ${}_L\Psi_2$ Weyl tensor component is equal to the mass density is consistent with the role Ψ_2 plays in the Bondi definition of the mass of an asymptotically flat space-time.

V. PROJECTION OF BIANCHI IDENTITIES

Each Bianchi identity, Eqs. 15-22, can be projected in a similar manner. While each identity holds under the projection when using the right hand sides of Eqs. 11 and 12, our interest is in forming field equations for the components of the Ricci tensor (or matter density) given the Weyl tensor (or gravitational shear) as a source under the conditions of gravitational lensing. This justifies throwing away boundary value terms or terms that are "small" under the projection relative to other quantities in the equation.

Under the projection, δ and $\bar{\delta}$ directional derivatives lie in the lens plane (to zeroth order in ζ) and the integration can be passed through the derivative. This implies, for example, that the projection of $\delta\Psi_1$ will be zero since the projection of Ψ_1 is zero. When the projection is applied to quantities on which the D and Δ derivative operators act, one has

$$ \int_{z_o}^{z_s} dz\, D\,\Phi_{11} = -\frac{1}{\sqrt{2}}\int_{z_o}^{z_s} dz \frac{\partial}{\partial z}\,\Phi_{11} \approx 0, \tag{31}$$

where we will assume that all the curvature tensors are approximately zero far from the lens.

For four of the Bianchi identities, Eqs. 16, 17, 20, and 21, the entire left hand side of the Bianchi identity "vanishes" under projection. This means that these equations have no content as field equations for projected Ricci or Weyl tensor components. The equality of the identity under the projection holds exactly because the small boundary value terms that we choose to neglect cancel the small projected term on the right hand side of the equation.

Using Eqs. 11, 12 and 14, one can see that the four remaining Bianchi identities represent two independent equations; Eq. 18 is equivalent to Eq. 19, and Eq. 15 is equivalent to Eq. 22. Under projection, these equations become

$$\delta\left(3\,{}_L\Psi_2 + 2\,{}_L\Phi_{11}\right) \;=\; 6\int_{z_o}^{z_s} dz\,\rho\Psi_1, \tag{32}$$

$$\delta\,{}_L\Phi_{00} - \bar{\delta}\,{}_L\Psi_0 \;=\; 4\int_{z_o}^{z_s} dz\,\rho\Psi_1. \tag{33}$$

Recall that our physical setup was to have a lens at $z = z_l$ and the observer at the origin. At the observer, ρ diverges because the past light-cone which generates the null tetrad has its apex at the observer. For physically reasonable gravitational potentials of the form $\varphi(|\vec{r}-\vec{r_l}|)$ far from the lens, the combination $\rho\Psi_1$ is non-zero but finite and small at the observer's location. In addition, because the physical gravitational potential will only be substantially different from zero near the lens, the combination $\rho\Psi_1$ is a nearly odd function in $z - z_l$ due to the z derivative in the definition of Ψ_1. Thus, the projection of $\rho\Psi_1$ is very small compared with individual terms on the left hand side of Eqs. 32 and 33 for physically reasonable models.

Neglecting these small terms, we see that Eq. 32 ceases to be a differential equation:

$$\delta\left(3\,{}_L\Psi_2 + 2\,{}_L\Phi_{11}\right) = 0 \Rightarrow 3\,{}_L\Psi_2 + 2\,{}_L\Phi_{11} = c \tag{34}$$

for some constant c. Using the definitions of the projection, Eqs. 29 and 30, we see that the constant is zero, and this equation has no implications for gravitational lensing.

The remaining Bianchi identity becomes

$$\delta\,{}_L\Phi_{00} = \bar{\delta}\,{}_L\Psi_0, \tag{35}$$

which is a field equation for the projected mass density, ${}_L\Phi_{00}$ or κ, with the observed gravitational shear, ${}_L\Psi_0 = \gamma_1 - i\gamma_2$, as a source. Eq. 35 was the field equation reported in Kling & Keith [4], so that the different choice of tetrad between the two papers was not important. In Kling & Keith [4], it is shown that Eq. 35 is equivalent to the integral equation, Eq. 26, by use of a Green's function on the sphere.

By applying the $\bar{\delta}$ operator to both sides of Eq. 35, a Poisson equation is obtained:

$$\bar{\delta}\delta\,{}_L\Phi_{00} = \frac{1}{2}\left(\frac{\partial^2}{\partial x^2} + \frac{\partial^2}{\partial y^2}\right){}_L\Phi_{00} = \bar{\delta}^2\,{}_L\Psi_0. \tag{36}$$

This partial different equation provides a straight-forward way to determine gravitational lensing mass maps from observed weak lensing shear. Equation 36 is fully accurate and consistent to first order in the gravitational potential. The source term, $\bar{\delta}^2\,\Psi_0$ is manifestly real when written in terms of the gravitational lensing observables γ_1 and γ_2. Using ${}_L\Psi_0 = \gamma_1 - i\gamma_2$, we have

$$\bar{\delta}^2\,{}_L\Psi_0 = \frac{1}{2}\left(\gamma_{1xx} - \gamma_{1yy} + 2\gamma_{2xy}\right) - \frac{i}{2}\left(\gamma_{2xx} - \gamma_{2yy} - 2\gamma_{1xy}\right). \tag{37}$$

Using the definitions of γ_1 and γ_2 (Eq. 25), one can show that the imaginary part of Eq. 37 will always be zero. Hence, the component of the projected Bianchi identity, Eq. 35, informs us that projected mass density is related to the weak lensing shears by

$$\Delta^2\,{}_L\Phi_{00} = \Delta^2\kappa = \kappa_{xx} + \kappa_{yy} = 2\bar{\delta}^2\,{}_L\Psi_0 = \gamma_{1xx} - \gamma_{1yy} + 2\gamma_{2xy}. \tag{38}$$

Hereafter, we will refer to the projected Ricci and Weyl tensor components ${}_L\Phi_{00}$ and ${}_L\Psi_0$ as the projected matter density and gravitational shears, κ and $\gamma_1 - i\gamma_2$.

VI. NUMERICAL METHODS

We examine the feasibility of integrating Eq. 38 by introducing a sample matter distribution and computing κ directly from Eq. 29 and indirectly from numerical integration. Our goal is to evaluate, under the simplest observational scenarios possible, whether numerical integration of Eq. 38 is a promising approach to determining accurate mass

maps. Keeping with the simple approach, we choose to use relaxation methods for our numerical integration based on Press et al. [8].

In relaxation methods, one attempts to set a grid spacing that is appropriate to the rate of change of the functions being integrated. However, we choose to constrain the grid spacing based on approximate number counts of objects in the background of a lens that are resolved by the telescope in question. Observational weak gravitational lensing is an inherently statistical study since the natural shape of unlensed background objects is not known and only assumed to be *on average* circular. For the purposes of this paper, we assume that there are not intrinsic background galaxy alignments.

Far from the center of a matter distribution, the gravitational lensing shear signal is weak, and a relatively large number of objects is required to form a good estimate of the underlying shear. Closer to the center of the distribution, a smaller number of objects is needed because the shear is substantially larger. Generally, 30-40 objects far from the center of the matter distribution and 10 objects in the central region are sufficient for a reasonable statistical weak lensing analysis.

For the purposes of our numerical tests, we consider that one can measure average values of γ_1 and γ_2 in each box and assign these to grid values. While we could compute analytic derivatives of γ_1 and γ_2 to use on the right hand side of Eq. 38, we will use numerical derivatives based on the grid values. Hence, as the grid spacing grows, precision will be lost in the source term of our Poisson equation. This is appropriate because we are attempting to model actual practice where the data must be binned to overcome the statistical nature of the measurements.

For our model, we consider a truncated isothermal sphere matter distribution with a core radius, whose three dimensional matter density is given by

$$\rho = \frac{\sigma_v^2}{2\pi\, G}\frac{1}{r_c^2 + r^2}\frac{r_t^2}{r_t^2 + r^2}, \tag{39}$$

where σ_v is the velocity dispersion and r_c and r_t are the core and tidal radii of the distribution. The model is inspired by the truncated NFW model proposed by Baltz et al [9], but yields simpler analytic expressions for the projected matter density and gravitational shear expressions than either NFW or truncated NFW models. For $r \ll r_t$, the model represents an isothermal sphere with a core radius. The total mass of the model (extended to infinity) is finite and is given by

$$M_{tot} = \frac{\pi r_t^2 \sigma_v^2}{G\,(r_c + r_t)}, \tag{40}$$

and the three-dimensional gravitational potential approaches a point mass potential for large r.

The projected mass density is

$$\Sigma = \int_{-\infty}^{\infty} dz\rho = \frac{\sigma_v^2}{2\,G}\frac{r_t^2}{r_t^2 - r_c^2}\left(\frac{1}{\sqrt{s^2 + r_c^2}} - \frac{1}{\sqrt{s^2 + r_t^2}}\right), \tag{41}$$

for the radial parameter $s = \sqrt{x^2 + y^2}$ in the lens plane. The projected gravitational potential, ψ found by integrating the two-dimensional Poisson equation and using the constants of integration to make the potential finite at the origin is

$$\psi = -\frac{2\pi\sigma_v^2\, r_t^2}{r_t^2 - r_c^2}\left[\sqrt{s^2 + r_t^2} - \sqrt{s^2 + r_c^2} + r_c \ln\left(\frac{r_c + \sqrt{s^2 + r_c^2}}{r_c}\right) - r_t \ln\left(\frac{r_t + \sqrt{s^2 + r_t^2}}{r_t}\right)\right]. \tag{42}$$

The Ricci tensor or κ, can be explicitly calculated from Eqs. 29 as

$$\kappa = -\frac{\pi\sigma_v^2\, r_t^2}{r_t^2 - r_c^2}\left(\frac{1}{\sqrt{s^2 + r_t^2}} - \frac{1}{\sqrt{s^2 + r_c^2}}\right). \tag{43}$$

The gravitational shears for this matter distribution are

$$\gamma_1 = -\left(\frac{\sigma_v^2 \pi r_t^2}{r_t^2 - r_c^2}\right)(y^2 - x^2)\mathcal{Q},$$
$$\gamma_2 = \left(\frac{\sigma_v^2 \pi r_t^2}{r_t^2 - r_c^2}\right)(2xy)\mathcal{Q}, \tag{44}$$

for

$$\mathcal{Q} = \frac{1}{\sqrt{s^2 + r_t^2}(r_t + \sqrt{s^2 + r_t^2})^2} - \frac{1}{\sqrt{s^2 + r_c^2}(r_c + \sqrt{s^2 + r_c^2})^2}, \tag{45}$$

and cartesian coordinates $\{x, y\}$ in the lens plane. We will compute γ_1 and γ_2 from Eq. 44 and assign these values to each grid point. We emphasize that we will take numerical derivatives of these values to simulate the case of observational data. We note that Poisson's equation is independent of σ_v, so that the relative errors we cite in this paper are invariant under scaling σ_v, which controls the mass of the cluster.

For our numerical modeling, we choose to set the core radius to 250 kpc and the tidal radius to 1.5 Mpc. The total mass of the cluster for a velocity dispersion of 1500 km s^{-1} is equal to 2.1×10^{15} solar masses. At a radius of 0.5 Mpc from the center, the ratio of the densities $\rho(r = 0.5\text{Mpc})/\rho(r = 0)$ is only 0.18, but 6.0 Mpc from the center, this ratio has fallen to 1.0×10^{-4}.

VII. NUMERICAL TESTS

In this section, we are interested in testing the integration of the Poisson equation, Eq. 38, under conditions representative of typical weak lensing measurements. We consider ground based observations by wide field telescopes, space based observations made by HST, and a hybrid, two-grid combination where one has both a quality ground and space based image.

As our primary comparison, we look at the scaled error in the projected mass density in each box, found by subtracting the value of κ found by numerical integration of Eq. 38 to the exact expression in Eq. 43 and dividing by the correct value of κ at the center. (The more common relative error is less meaningful, as it approaches one at the edges of the grid because we set the edge values to zero as the boundary condition, even though this is in fact a small error.) We also compare the total integrated masses, which we estimate as the sum of the mass densities in each box times the box area.

As an example of a standard ground-based, wide-field telescope usage, we consider the number counts and field of view (fov) for the DLS project reported in Wittman et al [10]. Here, 4-m class telescopes with 35 arc sec fov were used to observe five well separated fields for weak lensing signals. Filtering on well observed objects using the standard software for source extraction (SExtractor [11]) and shape measurement (ellipto [12]), yielded 20 objects per square minute. Assuming that a lens is at a redshift of 0.45 with minimal dithering of the stacked images, this translates into an observed lens plane that is approximately 12 Mpc across in the standard cosmology.

Hence, while one would like a smaller grid spacing for resolution, dividing the field of view into 25×25 boxes that are 0.48 Mpc across yields an appropriate average of 40 objects per box. Adding one out of field of view set of data points to which one can assign a boundary value of zero yields a 27×27 grid for relaxation of Eq. 38. We note that when computing numerical derivatives along the edges of the interior 25×25 grid, it is appropriate to use only the interior (measured data) points and not the added exterior edge.

Figure 1 shows the scaled error in the projected mass density computed between numerical integration of Eq. 38 and the exact value in Eq. 43 when the boundary of the 27×27 grid is set to zero. The error in the central bin (not shown in Figure 1) is +31%, but the errors in other bins are all small. Along the x axis passing through the center of the distribution, the numerical integration slightly overestimates the mass density for values near the center, whereas along the diagonal, the numerical integration always slightly underestimates the correct value. When the boundary values are set to the correct values, which one would never know in practice, there is no significant change in the error estimates, implying that assigning zero to the boundary is not a significant source of error. The total integrated mass, estimated as the sum of the mass density times the box area, from the numerical integration underestimates the total integrated mass by only 8.8%. This is in part because while the central mass density value is significantly underestimated, the numerical integration overestimates other boxes.

By setting the grid spacing to an arbitrarily small value, one can achieve good resolution. Using a 101×101 boxes for this field of view, corresponds to a grid spacing of 0.118 Mpc. For this spacing, the maximum relative error is in the central bin and is only 3.3%, and the total integrated mass is correct to 7.8%. Plots of the scaled error for

this number of boxes has the same general features as Fig. 1. Setting the added boundary values to the (in principle unknown) correct values results in extremely accurate numerical integration at this number of boxes, as one would expect.

Therefore, we see that the overall limitation is the requirement of large boxes. For the scenario we have described, using 101×101 boxes results in only 2.4 objects per box. We conclude that for ground-based, wide-field telescopes under normal operating conditions, numerical integration of Eq. 38 by relaxation with large boxes will be good enough to detect weak lensing and get a sense of the overall mass, but will be insufficient for detailed mass maps.

We also see that the mass sheet degeneracy is not a major issue for wide field images. Setting the edges to zero (as opposed to the unknown correct values) does not significantly effect the results. This is because the ratio of mass density at the edge of a wide field compared to the center is small.

For a space-based optical telescope such as the HST, a significantly higher number of background objects can be resolved, but the field of view is substantially smaller. Based on the HUDF number counts presented in Beckwith et al [13], one can expect 150 objects per square arc minute for the same cuts as are used for the DLS sample. The HST field of view is approximately 200 arc sec across, so that for a lens at a redshift of 0.45, the lens plane is only 1.14 Mpc by 1.14 Mpc. However, HST can resolve approximately 1100 background objects in this field of view. Dividing the HST image into $11 \times 11 = 121$ boxes results in a grid spacing of 0.104 Mpc with approximately 13 objects per box.

Because the mass density 0.5 Mpc from the center of a cluster is not close to zero, poor results are achieved when relaxing with zero as a boundary value. To see what one could achieve, we set the boundary values to the correct values and use relaxation to find the projected mass density. Figure 2 shows that the scaled error indicates that good modeling is possible if one knows the boundary values, with a maximum relative error of 3.0%. The scaled error curves have similar, but more gentle slopes to those of the wide-field telescopes. The total relative error in the mass is 1.3%.

This modeling is unphysical because one can never know the true mass density to assign at the boundary of the HST image. However, if one had both a ground-based, wide field image and an HST image of the same cluster, then one could use the wide-field image to give interpolated values for the boundary of the HST image.

To demonstrate the effectiveness of this approach, we assume that we have a wide field, ground based image and an HST image of the same system with the parameters above. We assume that the centers of these two images are the same and that there is no rotation between the images. After relaxing the wide field image using 25×25 boxes as before, we use the numerically obtained values of κ from the large grid to find values for the boundary of the HST image by interpolation. We then relax the small grid with these interpolated boundary values.

The relative error in the κ boundary values is shown in Fig. 3 along one line of the boundary of the small field of view grid. The points at large x correspond to the corners of the grid, and by design, the errors are symmetrical along each of the four edges of the small grid. We see that the approximate boundary values have a moderate relative error, where the relaxed values from the large grid slightly underestimate the true values near the corners of the grid by about 5% and substantially overestimate the values near the center of the grid by about 25%.

Even though the relative errors in the small grid boundary values are moderate, the actual errors are small compared to assigning zero on the boundary of the small grid. This results in successful relaxation of the small grid in reproducing the mass density. The error in the central bin is less than 1% and the total relative error in the predicted mass on the small grid is -3.1%. (The relaxed total mass is more than the actual value.)

Figure 4 shows the scaled errors along the x axis and diagonal as before. These scaled errors clearly track the error in the boundary conditions found by interpolation, as one would expect. Nevertheless, the errors are all acceptably small so that one can use the ground based image to provide boundary values and the space based image to provide accurate mapping of the mass density.

VIII. DISCUSSION

This paper includes a rigorous analysis of the Bianchi identity under the conditions of gravitational lensing leading to the derivation of a Poisson equation for the projected mass density in terms of derivatives of the observed lensing shear. Using the simplest possible numerical integration scheme, we show that it may be possible to use the Poisson equation to determine accurate mass maps when a ground-based, wide-field image and a high-resolution, space-based image of the same system are used in a two grid method.

Compared with an initial investigation of the Bianchi identity [4], this paper uses a more physical tetrad that makes manifest the connection to the light cone of the observer. In this way, the paper is more in the spirit of the non-perturbative approach initiated by Frittelli & Newman [14] and independently by Perlick [15]. The resulting differential relation, Eq. 35, found in both papers is derived here in a more rigorous fashion where all the relevant physical approximations are made.

One might have hoped that the other components of the Bianchi identity, not examined previously in this context, would have yielded new differential relations between observables. In particular, one might have suspected that a Bianchi identity component might have contained information regarding image magnification, which can also be tied to the mass density. We show that this is not the case, and that no new physical information is contained in the remaining seven Bianchi identity components.

A full non-perturbative treatment of image distortion is given in Frittelli et al. [7]. It is well known that the optical scalars, ρ and σ, which control the divergence and shearing of the pencil of rays connecting an extended source to the observer through the optical scalar equation, are related to the components of the Ricci and Weyl tensors through the Sach's equation. Frittelli et al. [7] show in detail how this leads to image distortion (both shearing and magnification).

The advance of this paper is to explicitly derive a relation between the mass density (represented by the Ricci tensor component ${}_L\Phi_{00}$) and the gravitational shears (represented by the Weyl tensor component ${}_L\Psi_0$). This connection is the meaningful observational relationship, but the fact that it comes directly from the Bianchi identity, rather than a manipulation of the optical scalar equations or the Sach's equation, would have to be viewed as a happy accident.

The Poisson equation derived here is related to the Poisson equation reported in Seitz et al. [3], which is derived kinematically by considering the relationships between κ, γ_1, and γ_2 and the underlying projected gravitational potential. When the terms that are not linear in the gravitational potential are removed from the Poisson equation in Seitz et al. [3], one obtains the Poisson equation reported here. Removing the non-linear terms is consistent with the linearized metric used here.

We examined reasonable observational scenarios in this paper and found that for a wide-field image alone, it would at least be difficult to use Eq. 38 to determine accurate mass maps. Here, we studied only relaxation methods, which require that the data be binned to achieve an acceptable average shear. It is possible that the more complicated to implement method of maximum likelihood, which can use individual data points, would result in an accurate mass map.

We were able to show that the combination of a ground-based, wide-field image and an HST image could be used to determine an accurate mass map in the central HST region. The fact that good results were achieved using relaxation methods indicates that the numerical integration of Eq. 38 is a promising road for weak lensing mass maps. When using a wide-field image, we examined the mass sheet degeneracy and found that knowing the correct boundary values did not significantly improve the accuracy of the mass maps.

Our paper did not consider several important sources of error. First, we did not add noise to the shear measurements, which would more accurately reflect the observational situation. The presence of small noise would make the errors in the two grid method larger, but we believe that our large box size (large enough to accommodate roughly 20 objects per box), would minimize this error. Second, we did not model missing data in our analysis. Bright nearby stars lead to saturation in regions on the ccd image, obscuring sometimes large regions and generally reducing the ability to extract background objects nearby. This would both add to the noise in the average boxed shear values and typically cause a handful of boxes to have no measured data. One could model these missing data points using surrounding data points if this was the case. Overall, we expect that these two sources of error would lead to a decrease in the effectiveness of the numerical integration, but would not cause the numerical integration to fail.

Two minor issues not examined here related to the ground and HST images are not expected influence the results of our study. First, the two images are unlikely to be exactly centered. Second, there is typically a rotation between the two images. Using common stars or bright objects, one can easily orient the two coordinate systems. It is then simply a matter of interpolating from the large grid onto the small grid boundary. Since ground based images are so much larger than HST images, the center offset would have a minimal impact. A rotation would cause the relative error of Fig. 4 to vary in position, but the overall effectiveness should be maintained.

IX. CONCLUSION

This paper gives a rigorous derivation of a Poisson equation, Eq. 38, that directly relates the mass density to derivatives of the weak lensing shears. We show that no new information is obtained by examining the remaining components of the Bianchi identity, so that the full theory of weak gravitational lensing and image distortion is most completely described by the optical scalar equations discussed in Frittelli et al. [7].

Using the simplest possible integration scheme, we show that the Poisson equation can be used to detect weak lensing signals, but fails to give accurate mass maps for wide-field, ground based images. However, simple relaxation methods were shown to be successful when a ground and HST image were both present. This method of determining the matter distribution could prove very useful in developing highly accurate mass maps.

Further examination of the Poisson equation is warranted. Specifically, it would be interesting to know whether maximum likelihood methods could yield accurate mass maps for ground based images alone. Also, the application of

the two grid method to mock background images that include appropriate levels of noise would solidify the usefulness of the method.

Acknowledgments

BC thanks the Bridgewater State College Adrian Tinsley Program for Undergraduate Research for a Summer Grant that enabled his participation in this project. We acknowledge Ren Li, whose initial examination of the Bianchi identity components during a senior independent study directed some of our results, and Dr. Ian Dell'Antonio of Brown University for helpful discussions related to number counts of the DLS survey.

APPENDIX: NP FORMULA

For completeness, in this appendix we briefly outline the calculation of the NP tetrad components of the Ricci and Weyl tensors and the spin coefficients. For the perturbed metric given by Eq. 2, the non-zero, first order Ricci and Weyl tensor components are given by

$$R_{00} = -\nabla^2\varphi \qquad R_{ii} = -\nabla^2\varphi, \tag{A.1}$$

with $\nabla^2 = \partial_x^2 + \partial_y^2 + \partial_z^2$, and

$$\begin{aligned} C_{0i0i} &= \frac{1}{3}\left(-3\varphi_{ii} + \nabla^2\varphi\right) & C_{0i0j} &= -\varphi_{ij} \quad i \neq j \\ C_{ijij} &= \frac{1}{3}\left(3\varphi_{kk} - \nabla^2\varphi\right) \quad i \neq j \neq k & C_{ijik} &= -\varphi_{jk} \quad i \neq j \neq k, \end{aligned} \tag{A.2}$$

where we use 0 for time and i, j, k for spatial components, ignoring the usual index conventions.

The NP tetrad components of the Weyl tensor are defined by

$$\Psi_0 = -C_{abcd}\ell^a m^b \ell^c m^d, \qquad \Psi_1 = -C_{abcd}\ell^a n^b \ell^c m^d,$$

$$\Psi_2 = -\frac{1}{2}\left(C_{abcd}\ell^a n^b \ell^c n^d - C_{abcd}\ell^a n^b m^c \bar{m}^d\right),$$

$$\Psi_3 = C_{abcd}\ell^a n^b n^c \bar{m}^d, \qquad \Psi_4 = -C_{abcd}n^a \bar{m}^b n^c \bar{m}^d, \tag{A.3}$$

and the tetrad components of the Ricci tensor are

$$\begin{aligned} \Phi_{00} &= -\frac{1}{2}R_{ab}\ell^a\ell^b, & \Phi_{10} &= -\tfrac{1}{2}R_{ab}\ell^a\bar{m}^b, & \Phi_{20} &= -\frac{1}{2}R_{ab}\bar{m}^a\bar{m}^b, \\ \Phi_{01} &= -\frac{1}{2}R_{ab}\ell^a m^b, & \Phi_{11} &= -\tfrac{1}{4}\left(R_{ab}\ell^a n^b + R_{ab}m^a\bar{m}^b\right), & \Phi_{21} &= -\frac{1}{2}R_{ab}n^a\bar{m}^b, \\ \Phi_{02} &= -\frac{1}{2}R_{ab}m^a m^b, & \Phi_{12} &= -\tfrac{1}{2}R_{ab}n^a m^b, & \Phi_{22} &= -\frac{1}{2}R_{ab}n^a n^b, \\ & & \Lambda &= \tfrac{1}{24}R. \end{aligned} \tag{A.4}$$

Given the tetrad vectors in Eqs. 6-8, one can show that the tetrad components of the Ricci tensor are independent of ζ, with $\Phi_{00} = \Phi_{22} = 2\Phi_{11} = (1/2)\nabla^2\varphi$ as the only non-zero components. The tetrad components of the Weyl tensor are not independent of ζ, but to zeroth order in ζ are given in Eq. 12.

The NP spin coefficients are named, complex combinations of the Ricci rotation coefficients. They are defined by

$$\begin{aligned} \rho &= \ell_{a;b}m^a\bar{m}^b, & \sigma &= \ell_{a;b}m^a m^b, & \kappa &= \ell_{a;b}m^a\ell^b, & \tau &= \ell_{a;b}m^a n^b, \\ \mu &= -n_{a;b}\bar{m}^a m^b, & \lambda &= -n_{a;b}\bar{m}^a\bar{m}^b, & \nu &= -n_{a;b}\bar{m}^a n^b, & \pi &= -n_{a;b}\bar{m}^a\ell^b, \\ \epsilon &= \frac{1}{2}\left(\ell_{a;b}n^a\ell^b - m_{a;b}\bar{m}^a\ell^b\right), & \alpha &= \frac{1}{2}\left(\ell_{a;b}n^a\bar{m}^b - m_{a;b}\bar{m}^a\bar{m}^b\right), \\ \gamma &= -\frac{1}{2}\left(n_{a;b}\ell^a n^b - \bar{m}_{a;b}m^a n^b\right), & \beta &= -\frac{1}{2}\left(n_{a;b}\ell^a m^b - \bar{m}_{a;b}m^a m^b\right). \end{aligned} \tag{A.5}$$

We are interested in the spin coefficients for the flat background metric. To compute the spin coefficients, it is simplest to change coordinates to $(t, r, \zeta, \bar{\zeta})$ where the flat metric takes the form

$$ds^2 = dt^2 - dr^2 - \frac{4\,r^2\,d\zeta\,d\bar{\zeta}}{(1+\zeta\bar{\zeta})^2}, \tag{A.6}$$

and the null tetrad is given by

$$\ell^a = \left(\frac{-1}{\sqrt{2}}, \frac{1}{\sqrt{2}}, 0, 0\right), \qquad n^a = \left(\frac{-1}{\sqrt{2}}, \frac{-1}{\sqrt{2}}, 0, 0\right)$$
$$m^a = \left(0, 0, \frac{1+\zeta\bar{\zeta}}{\sqrt{2}\,r}, 0\right), \qquad \bar{m}^a = \left(0, 0, 0, \frac{1+\zeta\bar{\zeta}}{\sqrt{2}\,r}\right).$$

Although the connection for the flat metric, Eq. A.6, is not zero, then zeros in the components of the tetrad vectors in the $(t, r, \zeta, \bar{\zeta})$ coordinate system make computing the spin coefficients much simpler. The non-zero spin coefficients are

$$\rho = \mu \;=\; -\frac{1}{\sqrt{2}r}, \tag{A.7}$$

$$\alpha = \frac{\zeta}{2\,\sqrt{2}\,r} \qquad \beta\frac{-\bar{\zeta}}{2\,\sqrt{2}\,r}. \tag{A.8}$$

Only ρ and μ are zeroth order in ζ.

---

[1] Newman, E.T. & Penrose, R., J. Math Phys. **3**, 566-78 (1962)
[2] Miralda-Escude, J., IAU Symp. **173**, 131 (1996)
[3] Seitz, C. & Schneider, P., A&A 374, 740 (2001)
[4] Kling, T.P. & Keith, B., CQG **22**, 2921-2932 (2005)
[5] Newman, E.T. & Tod, K.P., *General Relativity and Gravitation: One Hundred Years after Einstein, vol 2*, (Perseus Publishing, New York, 1980)
[6] Schneider, P., Ehlers, J. & Falco, E.E., *Gravitational Lenses,* (Springer-Verlag, Berlin, Heildelerg, 1992)
[7] Frittelli, S., Kling, T.P., & Newman, E.T., Phys. Rev. D , **63**, 023007 (2001)
[8] Press, W.H. et al., 1995, *Numerical Recipes*, Cambridge University Press
[9] Baltz, E. et al., 2007, from arXiv:astro-ph:0705.0682.v2
[10] Wittman, D. et al., ApJ 643, 128 (2006)
[11] Bertin, E. & Arnouts, S., 1996, A&A Sup Ser 117, 393
[12] Bernstein, G.M. & Jarvis, M., 2002, AJ, 123, 583B
[13] Beckwith et al., AJ 132, 5 (2006)
[14] Frittelli, S., & Newman, E.T., Phys. Rev. D , **59**, 124001 (1999)
[15] Perlick, V., Living Rev. Relativity 7, 9. http://www.livingreviews.org/lrr-2004-9 cited on June 17, 2008

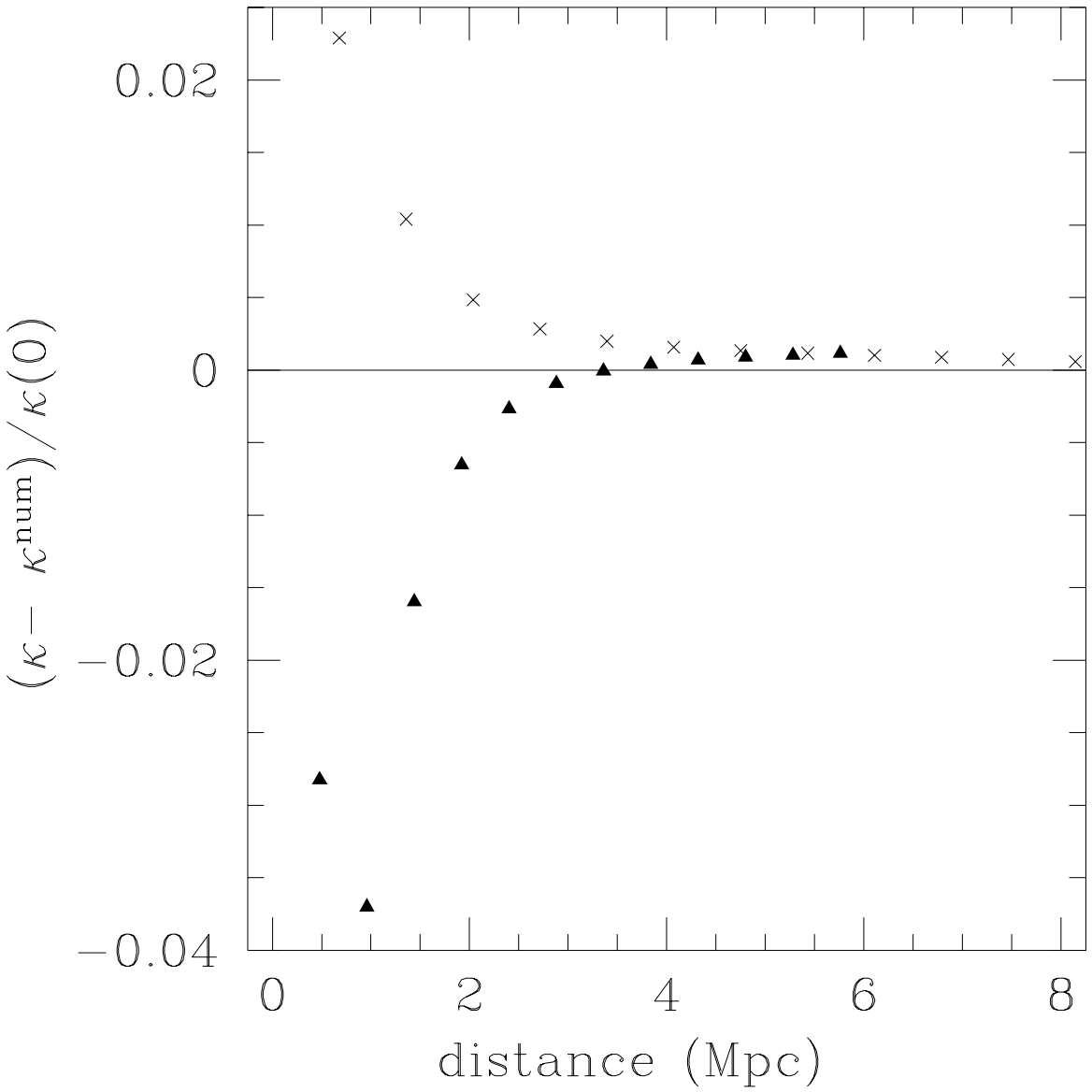

FIG. 1: The error in the projected mass density scaled by the value of κ at the origin for a wide field image with grid separation of 0.48 Mpc. The triangles represent the grid points along the x axis passing through the origin, while the crosses represent the grid points along the diagonal.

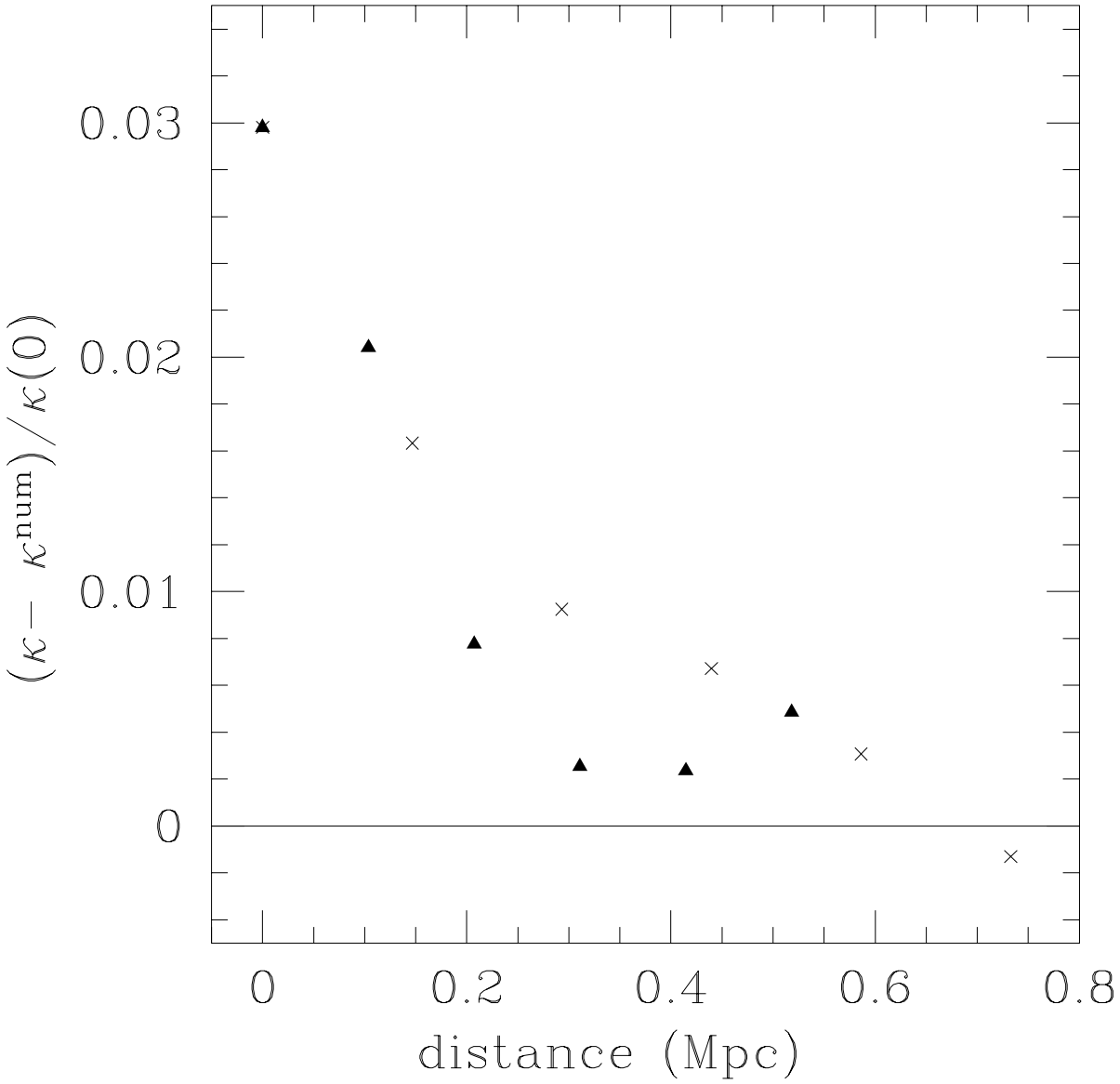

FIG. 2: The error in the projected mass density scaled by the value of κ at the origin for an HST image with grid separation of 0.104 Mpc. The boundary of the grid has been set to the (unknown) correct values. The triangles represent the grid points along the x axis passing through the origin, while the crosses represent the grid points along the diagonal.

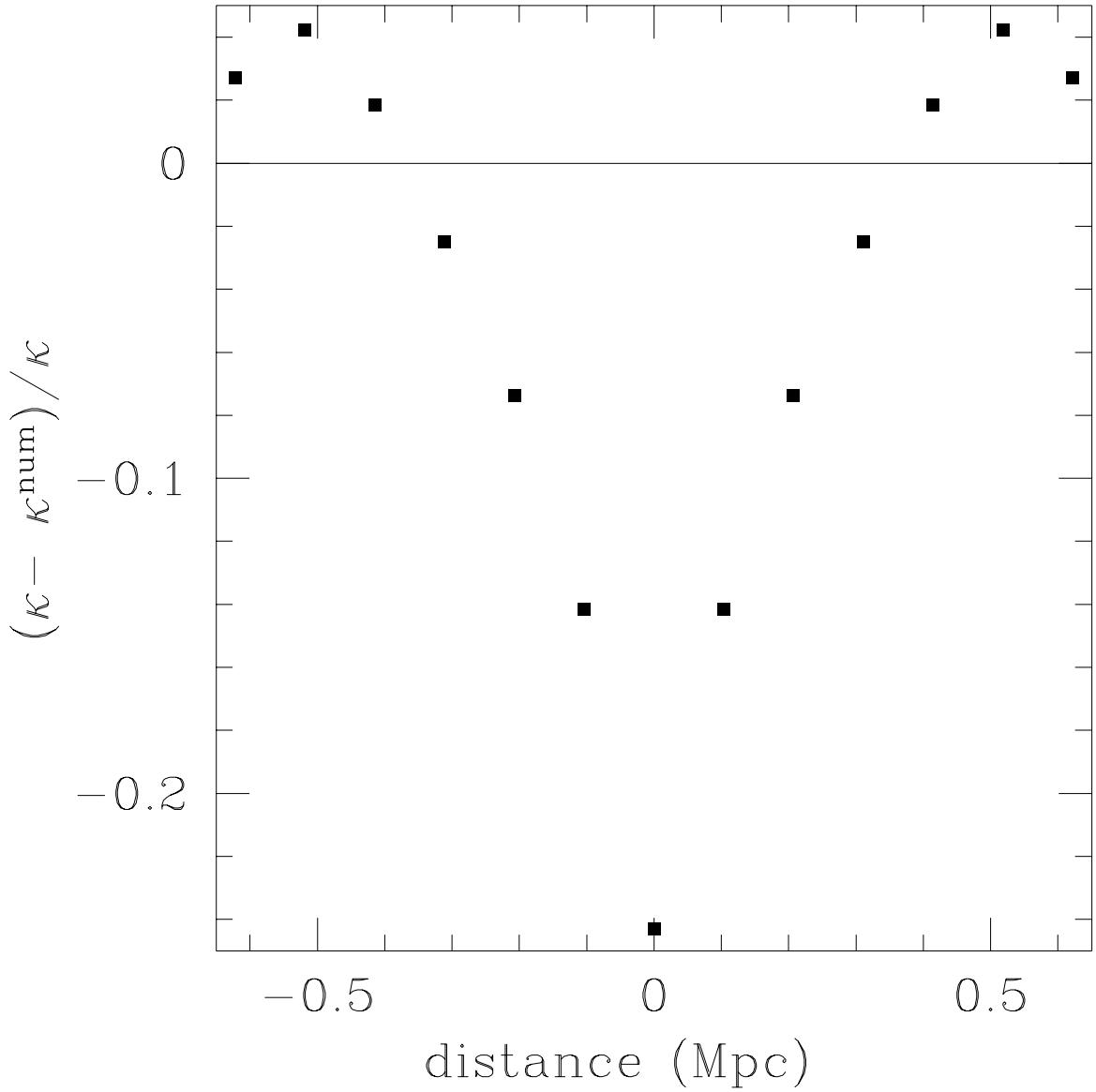

FIG. 3: The relative error in the projected mass density along the boundary of an HST image between the true values and values interpolated from a wide field image with a grid spacing of 0.48 Mpc.

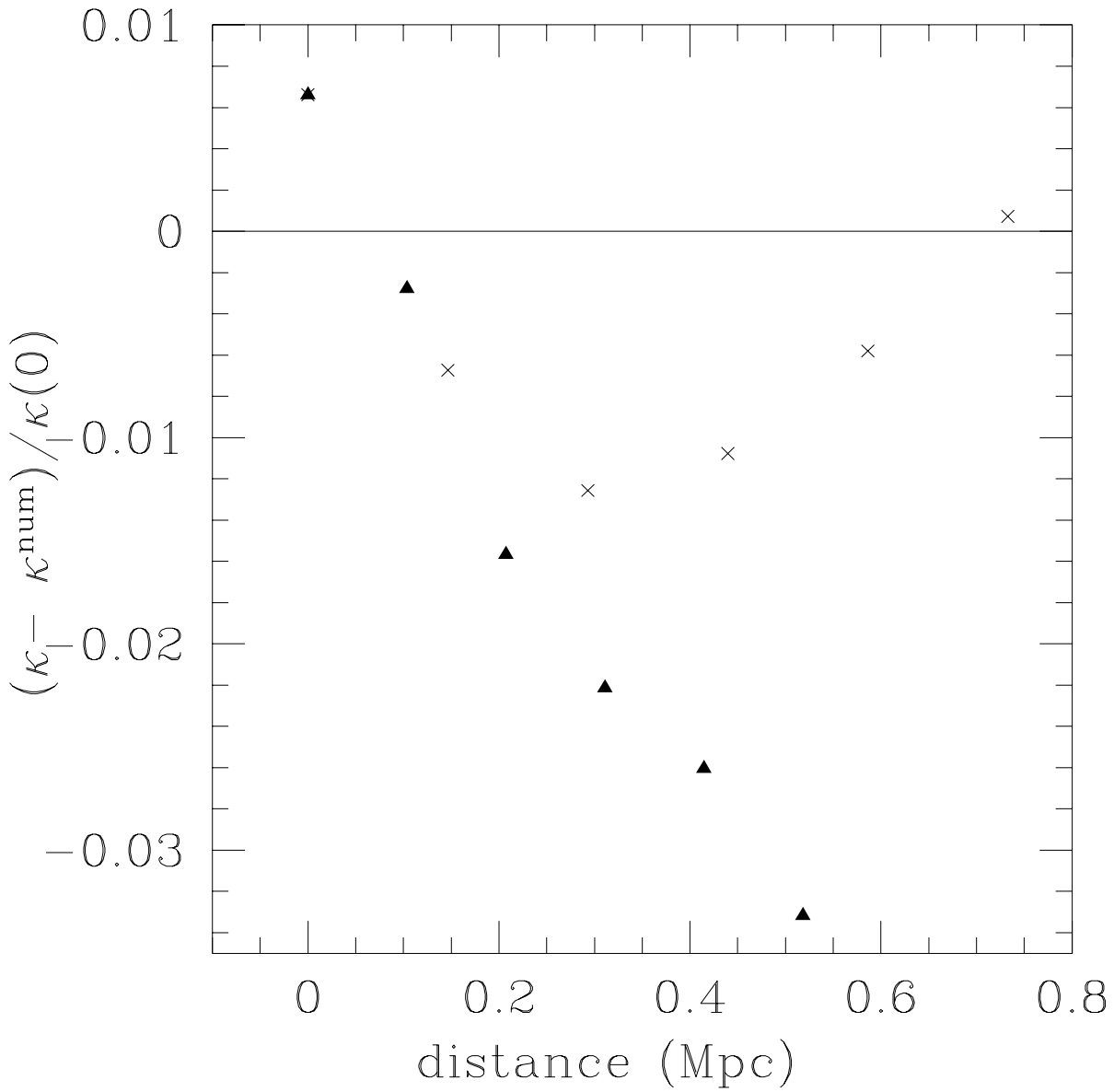

FIG. 4: The error in the projected mass density scaled by the value of κ at the origin for an HST image with grid separation of 0.48 Mpc where the boundary values are determined by interpolation from a wide field image. The triangles represent the grid points along the x axis passing through the origin, while the crosses represent the grid points along the diagonal.